Electronic Supplementary Material (ESI) for ChemComm.

Supplementary Materials

Unlocking the potential of NiMo foam substrate for water splitting using an ultrafast two-step dipping strategy

Experimental section

Materials

NiMo foam (porosity: 75%, pore density: 50 PPI ~130 PPI, thickness: 1.6 mm) was purchased from Suzhou Shenglongbao. Commercial Ni foam was purchased from Suzhou Jiashide Co., Ltd. Potassium hydroxide and ethanol were purchased from Shanghai LingFeng Chemical Reagent Co., Ltd. Acetone was purchased from Sinopharm Chemical Reagent Co., Ltd. Sodium hydroxide was purchased from Shanghai Zhanyun Chemical Co., Ltd. Iron (III) nitrate nonahydrate [$Fe(NO_3)_3$ $9H_2O$] was purchased from Sinopharm Chemical Reagent Co., Ltd. All reagents were analytical grade and used without further purification. All experimental water was purified using Millipore system catalyst.

Preparation of OH^-&Fe^{3+}-NMF Electrode

The NiMo foam (NMF, 1 cm × 2 cm) was dipped in 0.4 M Fe[$(NO_3)_3 \cdot 9H_2O$] solution for 3s, then quickly removed and air dried for 10 min. Then the precursor (Fe^{3+}-NMF) was dipped in 2.5M NaOH solution for 3s, then quickly removed and air dried for 5min, and then thoroughly cleaned with deionized water and ethanol. The final electrode (OH^-&Fe^{3+}-NMF) was obtained by drying in a drying oven at 60℃.

Preparation of OH^-&Fe^{3+}-NF Electrode

As a control sample, the same experimental conditions as the synthetic OH^-&Fe^{3+}-NMF were used for preparation, and only NiMo foam was changed into Ni foam (NF).

Preparation of NMF and NF Electrodes

Also as two control samples, NiMo foam (NMF) and Ni foam (NF) were cleaned

by sonicating in acetone solution for 10 min and then washed three times with ethanol and distilled water. At last, they were dried in a drying oven at 60 ℃.

Materials Characterizations

The morphology of the electrodes was observed by Zeiss Ultra 55 field emission scanning electron microscope (SEM), and elemental analysis was performed by energy dispersive X-ray (EDX) spectrum. Transmission electron microscopy (TEM, JAPAN-JEOL-JEM 2100 F), High-resolution TEM (HRTEM), and selected area electron diffraction (SAED) images were characterized at 200 kV accelerating voltage. Raman spectra were recorded using a Horiba LabRAM HR Evolution spectrometer under an excitation of 532 nm laser. X-ray photoelectron spectroscopy (XPS) analysis was carried out on ESCALab MKII spectrometer, which uses Mg Ka X-ray as the source of excitation. X-ray diffraction (XRD) was performed by using a Rigaku SmartLab, operated at 40 kV and 44 mA, parallel beam mode, λ=1.54 Å and scan rate 5 degree/min to investigate the crystal structure of electrodes.

Electrochemical Measurement

All electrochemical measurements were performed in a three-electrode system through the electrochemical workstation (CHI 660E) at room temperature. Hg/HgO and Pt sheets were employed as the counter electrodes. OH^-&Fe^{3+}-NMF, OH^-&Fe^{3+}-NF, NMF, and NF was used as the working electrode, respectively. The scanning rate of linear scanning voltammetry (LSV) was 5mV s^{-1}. Measurements were conducted in 1 M KOH solution, and the working electrode was controlled at 1×1 cm. All of the measured potentials (vs.Hg/HgO) were converted to the potentials against the

reversible hydrogen electrode (RHE) by Nernst equation $E_{RHE}=E_{Hg/HgO}+0.098+0.0591\times pH$. Electrochemical impedance spectroscopy (EIS) was measured by applying the AC voltage of 5mV in the frequency range from 100 kHz to 0.01 Hz. The electrochemically active surface area (ECSA) curve was measured by different scanning rates (50, 60, 70, 80, and 100mV s^{-1}). There was no Faraday reaction in the voltage range from 0.723 to 0.825 V. The capacitive current of the cyclic voltammetry curve ($\Delta J_{|Ja-Jc|}/2$) was drawn to fit the double-layer capacitance (C_{dl}), which is proportional to the surface area of the electrode. The ECSA was calculated according to the following Eq.1:

$$ECSA=\frac{C_{dl}\times A}{C_s} \quad \text{Eq.1}$$

where A is the geometric area of the electrode (1 cm^2 in our case), and C_s is constant. All presented potentials were corrected against the ohmic potential drop with 85% iR compensation.

Supplementary Figures

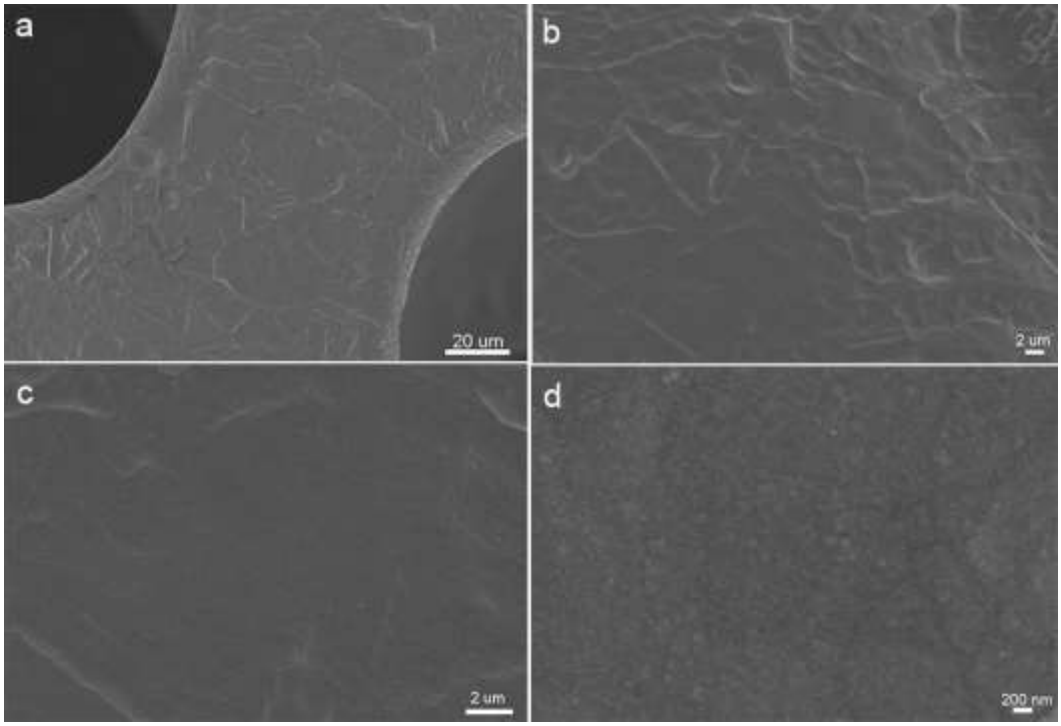

Fig. S1 Scanning electron microscopy images of NMF.

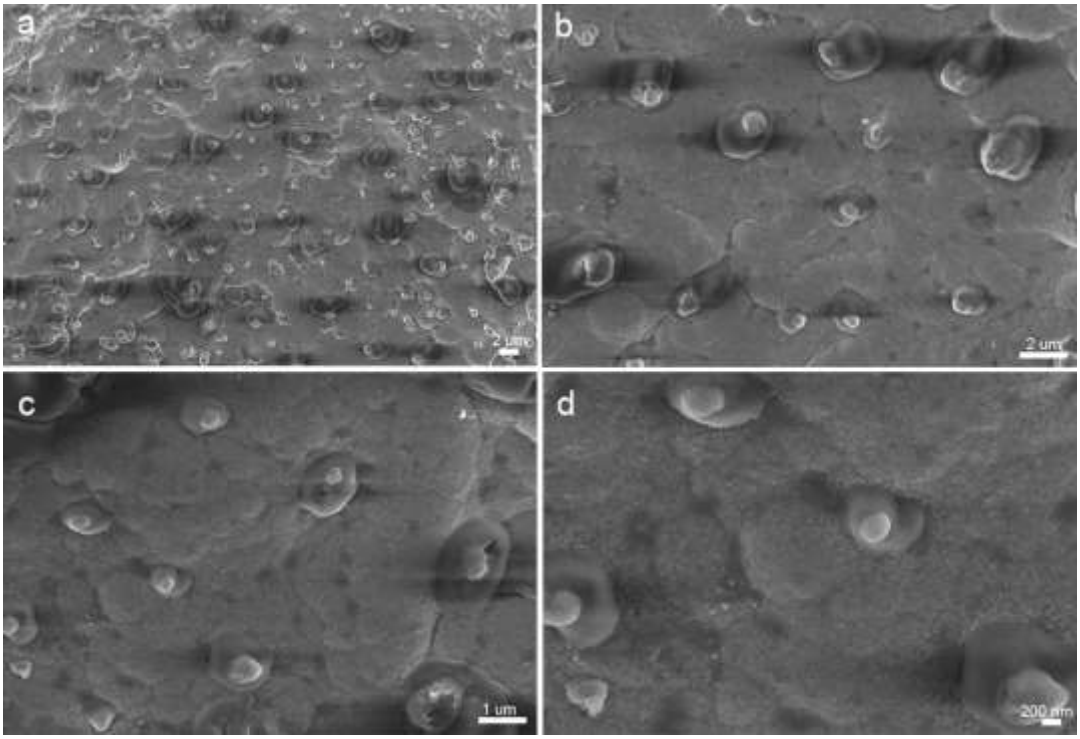

Fig. S2 Scanning electron microscopy images of Fe^{3+}-NMF.

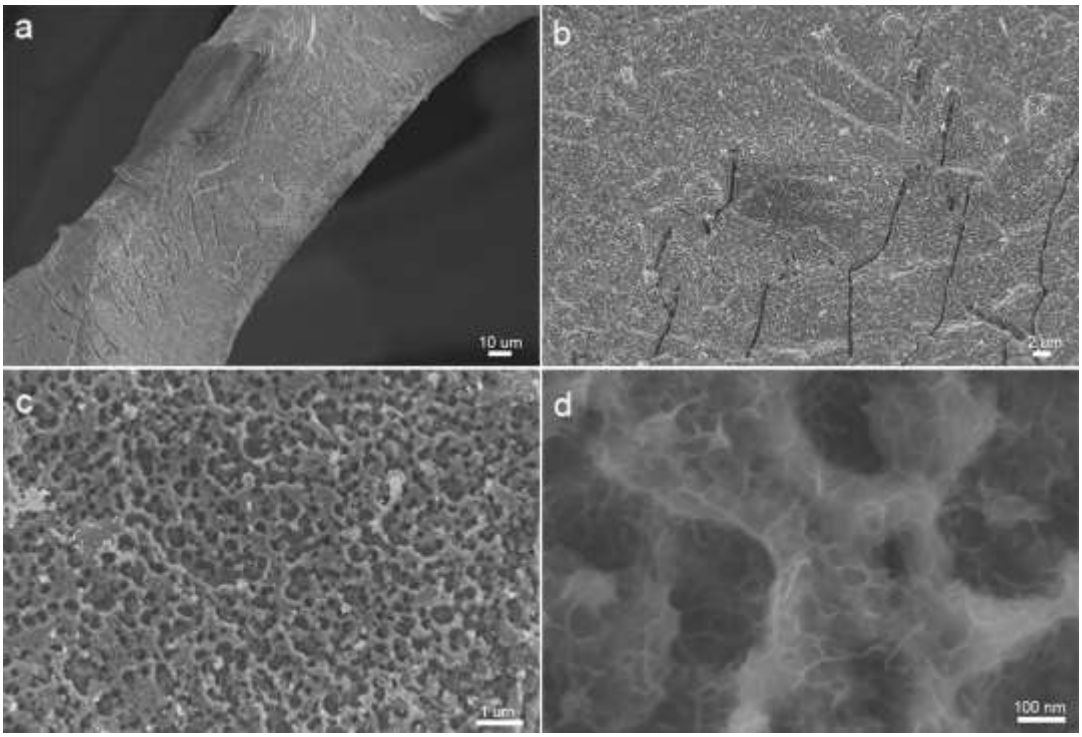

Fig. S3 Scanning electron microscopy images of OH^-&Fe^{3+}-NMF.

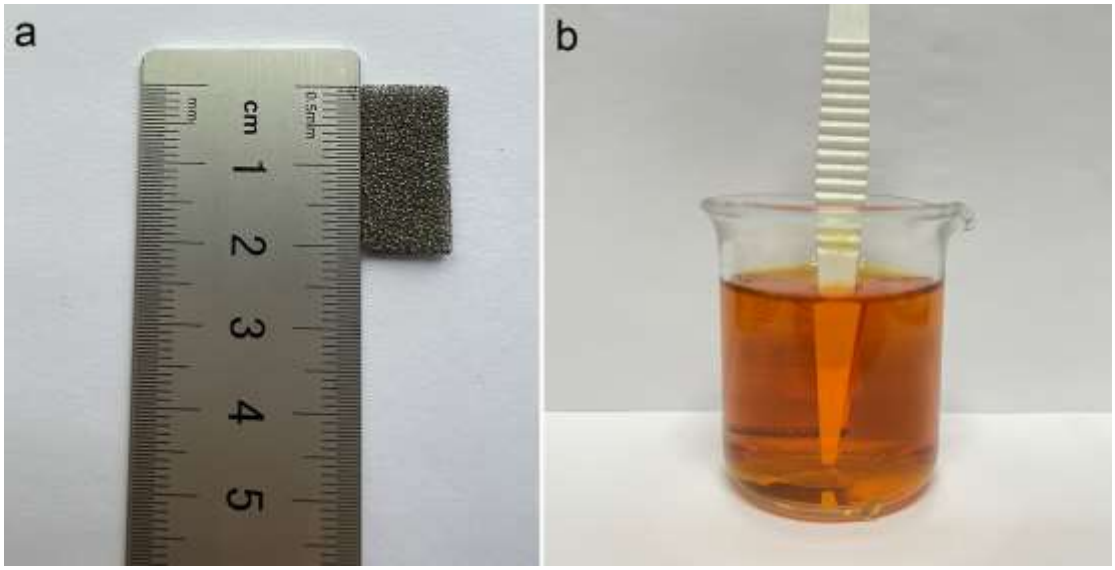

Fig. S4 Optical images of (a) NMF electrode and (b) immersed in 0.4M $Fe(NO_3)_3$ solution.

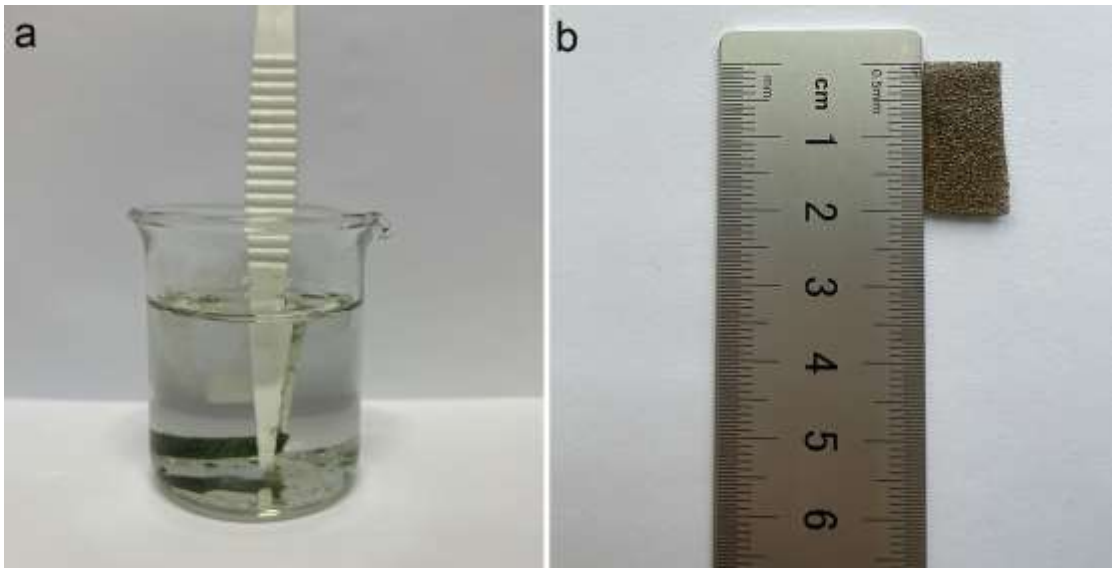

Fig. S5 Optical images of immersed in 2.5M NaOH solution (a) and (b) OH^-&Fe^{3+}-NMF electrode.

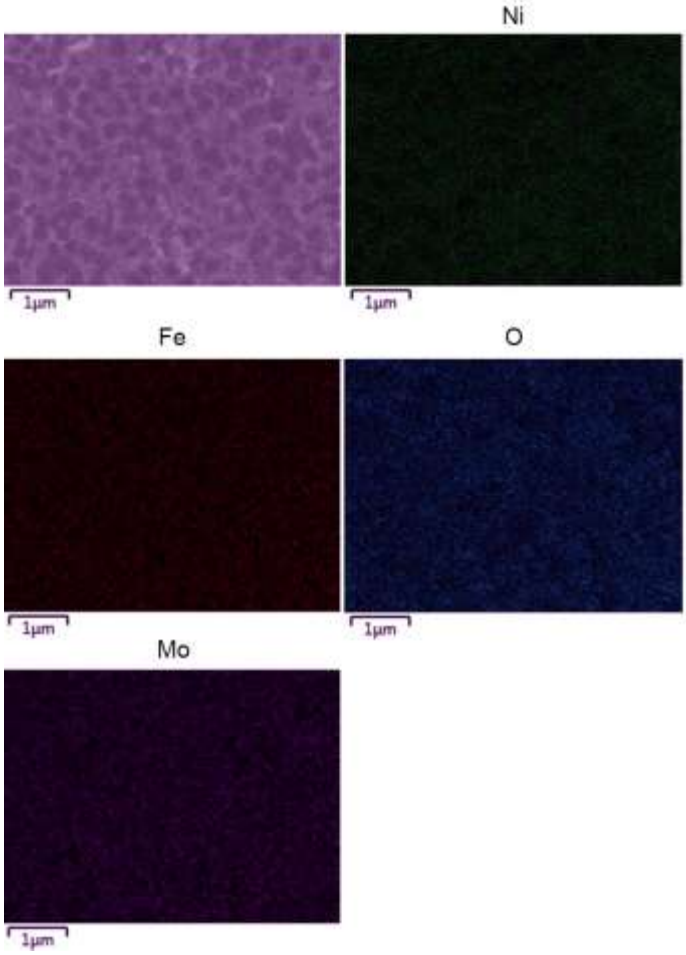

Fig. S6 EDS element mapping images of Ni, Fe, O and Mo for the OH^-&Fe^{3+}-NMF.

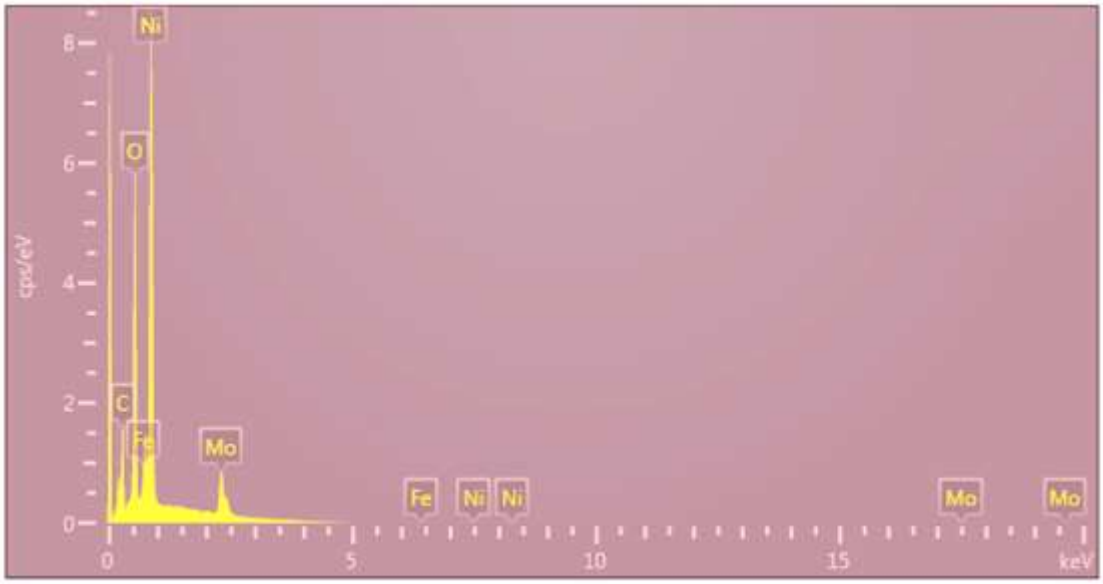

Fig. S7 EDX spectrum of OH^-&Fe^{3+}-NMF.

Element	Wt%	At%
Ni	54.8	41.6
Fe	4.7	3.8
O	15.4	42.9
Mo	25.1	11.7

Fig. S8 The corresponding element content of OH^-&Fe^{3+}-NMF.

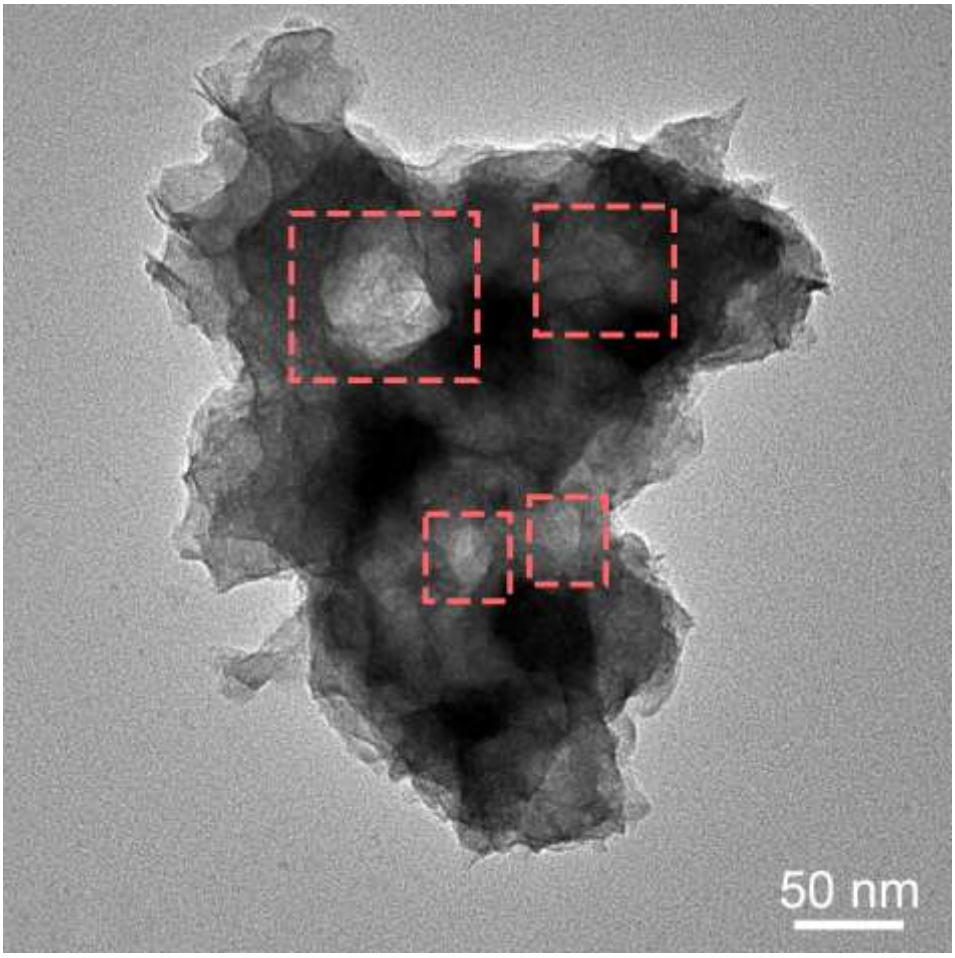

Fig. S9 TEM image of OH^-&Fe^{3+}-NMF.

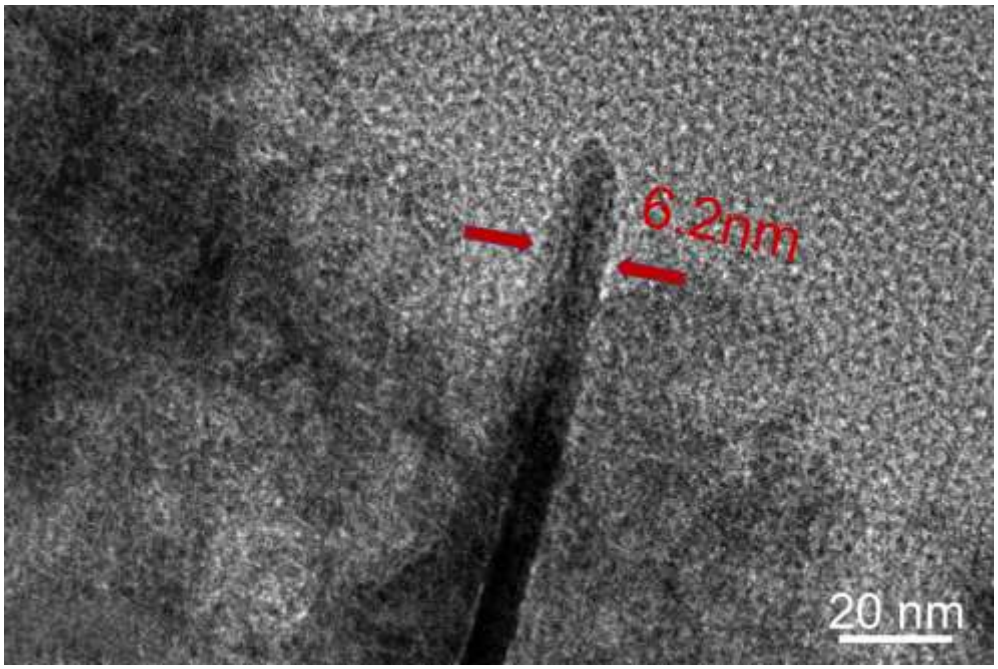

Fig. S10 HRTEM image of OH^-&Fe^{3+}-NMF.

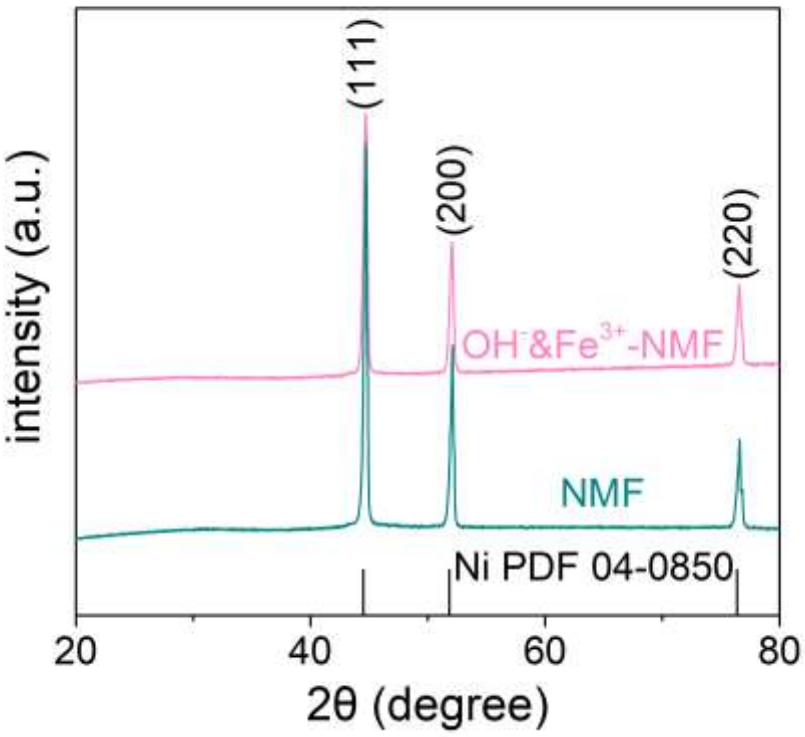

Fig. S11 XRD patterns of NMF and OH^-&Fe^{3+}-NMF.

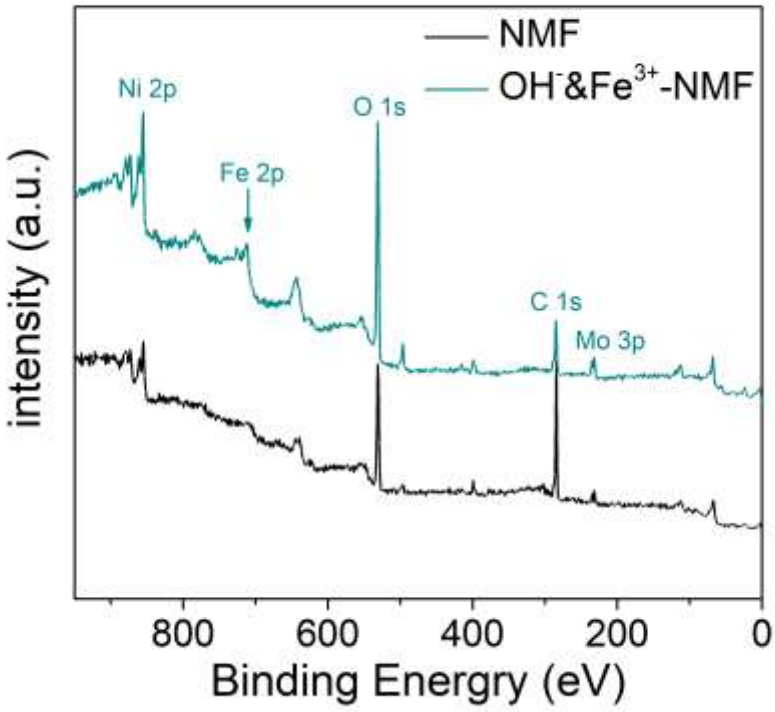

Fig. S12 XPS survey spectrum of NMF and OH^-&Fe^{3+}-NMF.

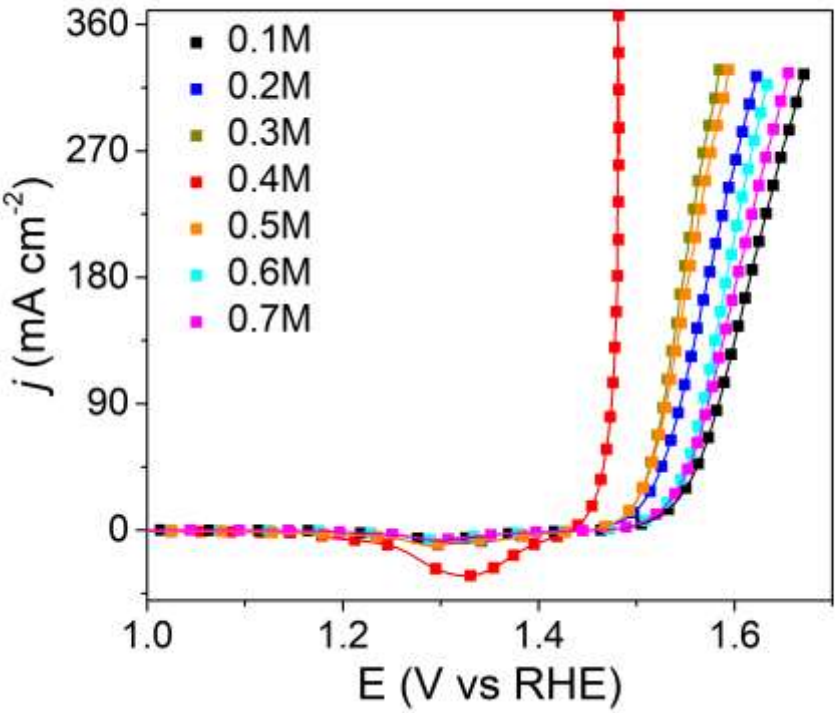

Fig. S13 LSV curves of electrodes prepared with various concentrations of $Fe(NO_3)_3$.

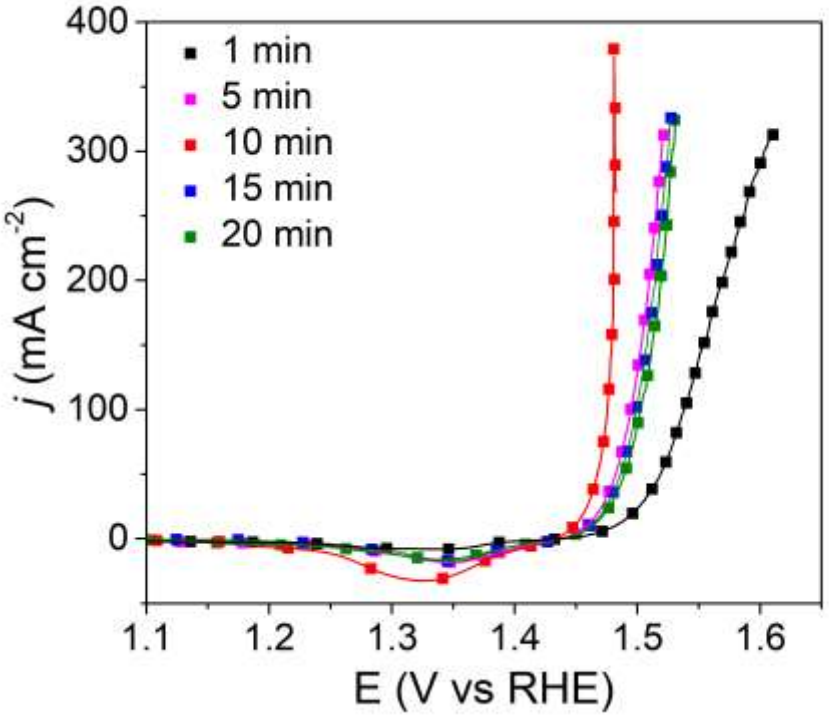

Fig. S14 LSV curves of electrodes at different drying times after the first dipping in 0.4 M $Fe(NO_3)_3$.

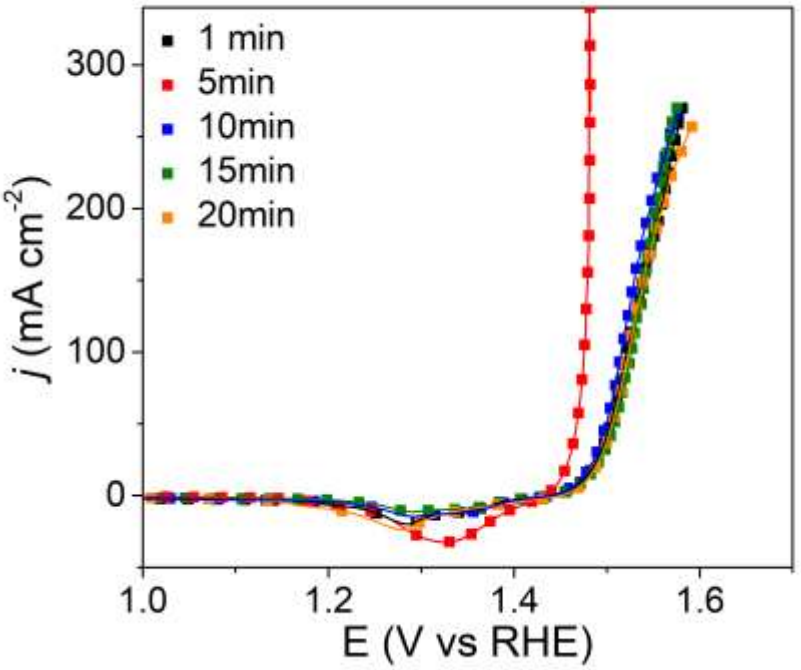

Figure S15 LSV curves of electrodes at different drying times after the second dipping in 2.5 M NaOH.

Firstly, we investigated the influence of the concentration of Fe^{3+} in the first dipping process. We only changed the concentration of Fe^{3+} and other conditions were remained constant. As shown in Fig. S13, the activity of the obtained electrode was very poor due to the low concentration of Fe^{3+} (0.1 M). As the concentration of Fe^{3+} increased to 0.4 M, the corresponding performance increased to maximum and then began to decline with the higher concentration of Fe^{3+}.

Secondly, we investigated the influence of the drying time after the first dipping in Fe^{3+}. We altered the drying time and other conditions were also remained constant. As shown in Fig. S14, the activity of the obtained electrode increased significantly with the dry time from 1 to 10 min. Thereafter, a downward trend appeared. When this drying time exceeded 15 min, the corresponding performance kept almost unchanged.

Thirdly, we continued to investigate the influence of the drying time after the

second dipping in OH^-. We altered the drying time and other conditions were also remained constant. As indicated in Fig. S15, with the increasing of drying time, the LSV curve firstly climbed and then dropped. The optimal electrocatalytic performance was achieved when the drying time was 5 min. When this drying time exceeded 10 min, the corresponding performance also kept almost unchanged. Collectively, the regulation of various parameters during electrode preparation was very important to find the optimal strategy.

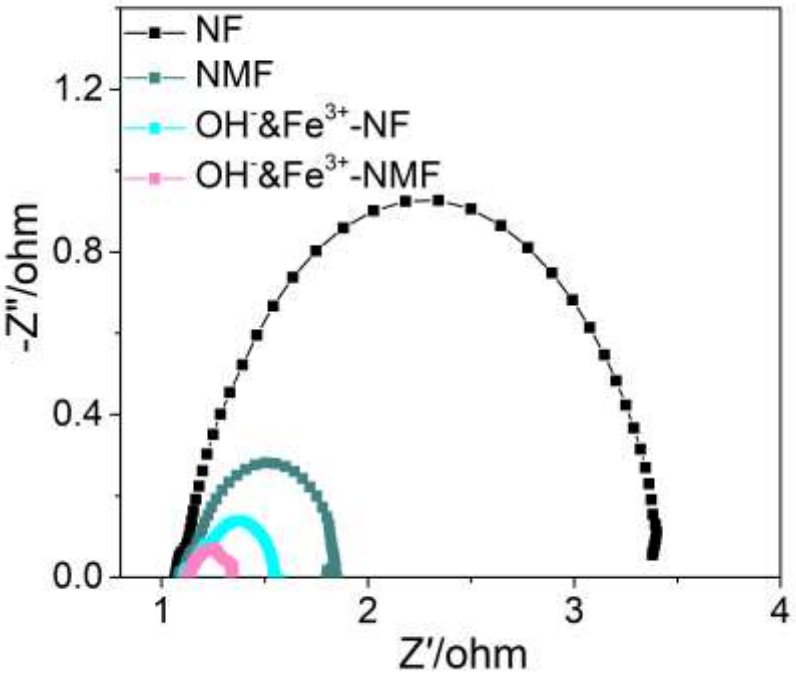

Fig. S16 Nyquist plots of different electrodes for OER.

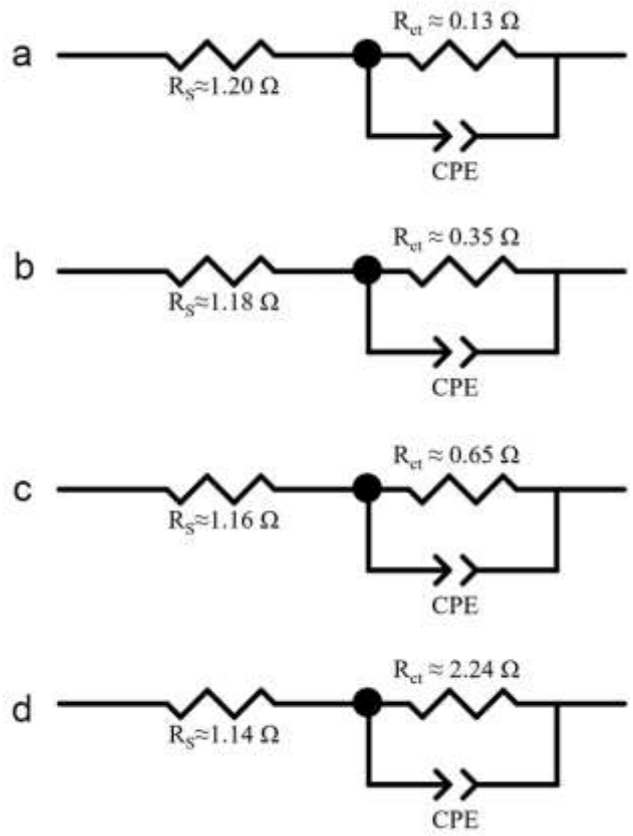

Fig. S17 Equivalent circuit diagram used for fitting impedance spectrum and the corresponding fitting results for OER: (a) OH^-&Fe^{3+}-NMF, (b) OH^-&Fe^{3+}-NF, (c) NMF and (d) NF. (Rs: equivalent series resistance, Rct: charge transfer resistance, CPE: constant phase angle element.)

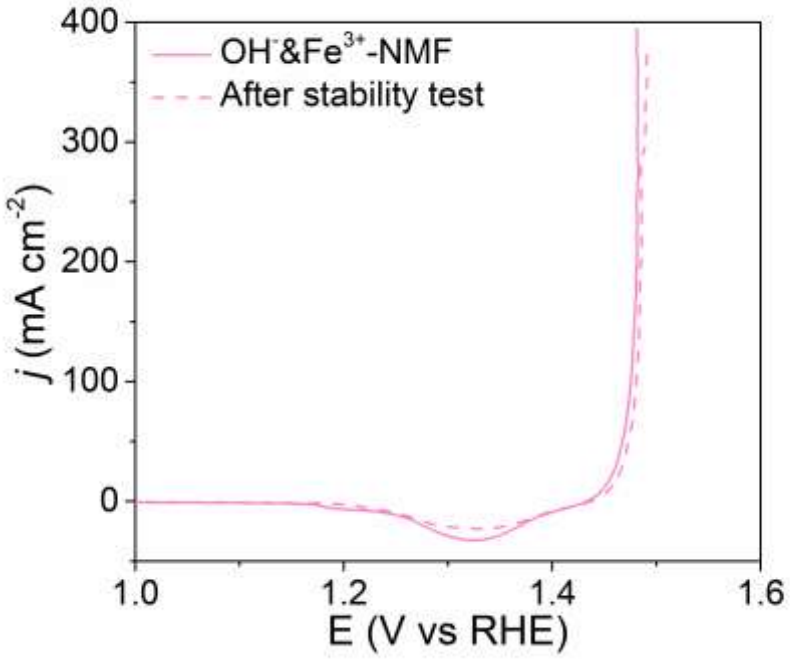

Fig. S18 Polarization curve of OH^-&Fe^{3+}-NMF after OER stability test for 120 h at current density of 100 mA cm^{-2}.

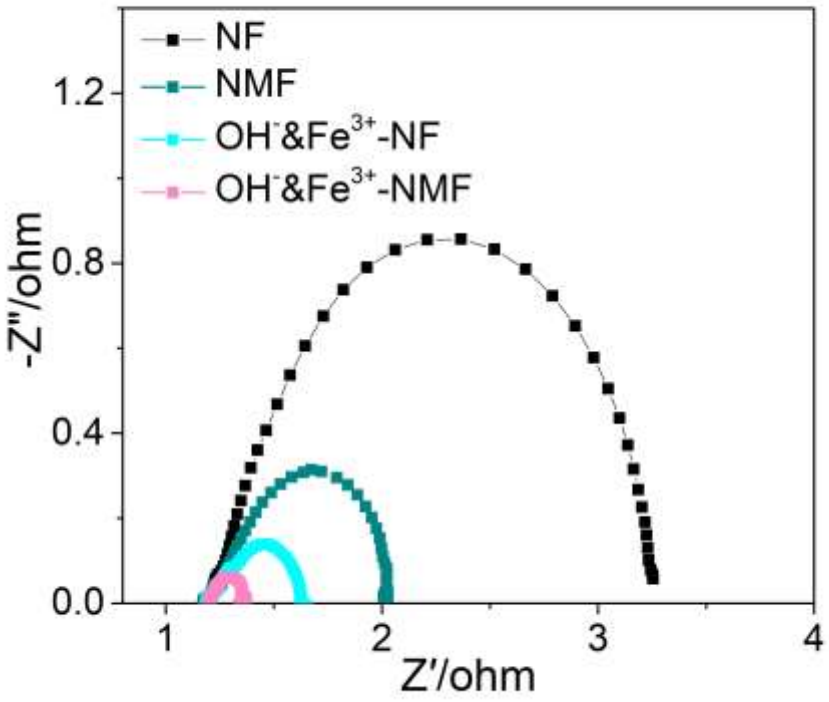

Fig. S19 Nyquist plots of different electrodes for HER.

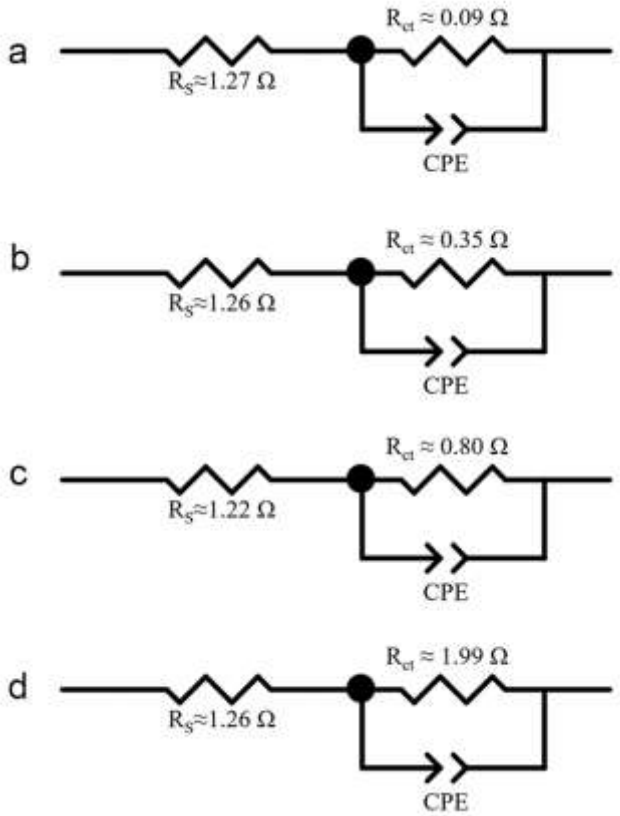

Fig. S20 Equivalent circuit diagram used for fitting impedance spectrum and the corresponding fitting results for HER: (a) OH^-&Fe^{3+}-NMF, (b) OH^-&Fe^{3+}-NF, (c) NMF and (d) NF. (Rs: equivalent series resistance, Rct: charge transfer resistance, CPE: constant phase angle element.)

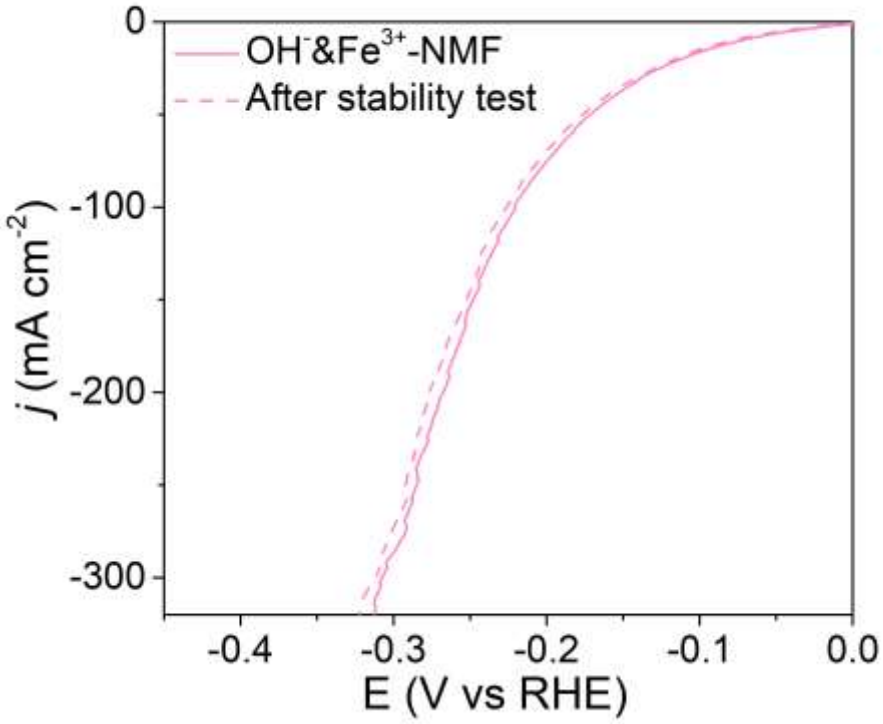

Fig. S21 Polarization curve of OH^-&Fe^{3+}-NMF after HER stability test for 120 h at current density of 100 mA cm^{-2}.

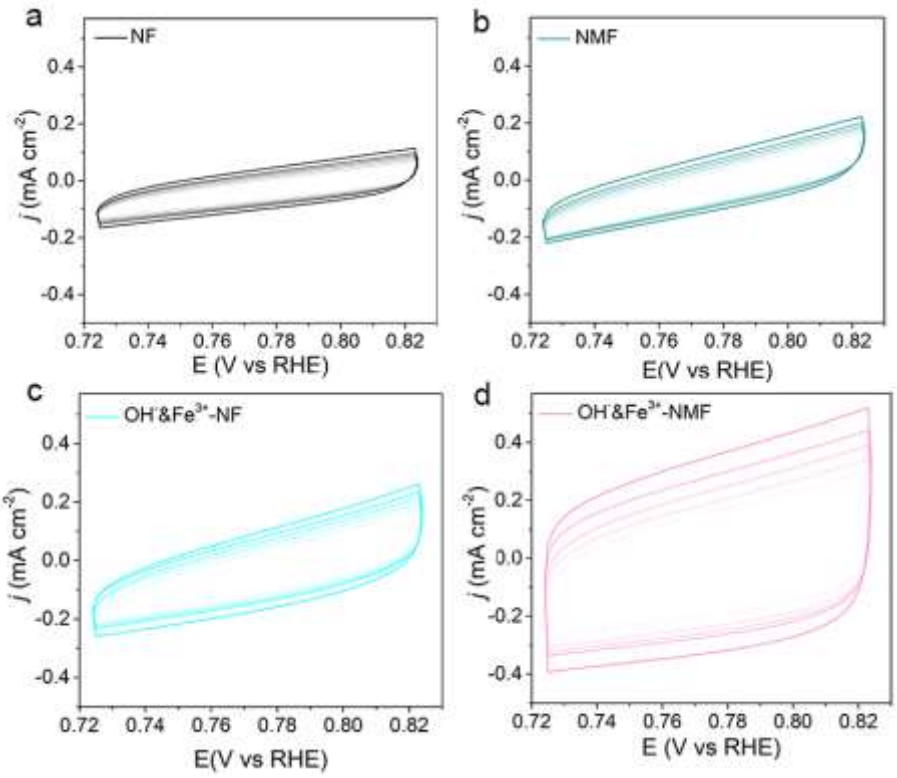

Fig. S22 CV curves measured at different scan rates from 50, 60, 70, 80, 100 mV s^{-1} (the color changes from light to dark) of (a) NF, (b) NMF, (c) OH^-&Fe^{3+}-NF, and (d) OH^-&Fe^{3+}-NMF.

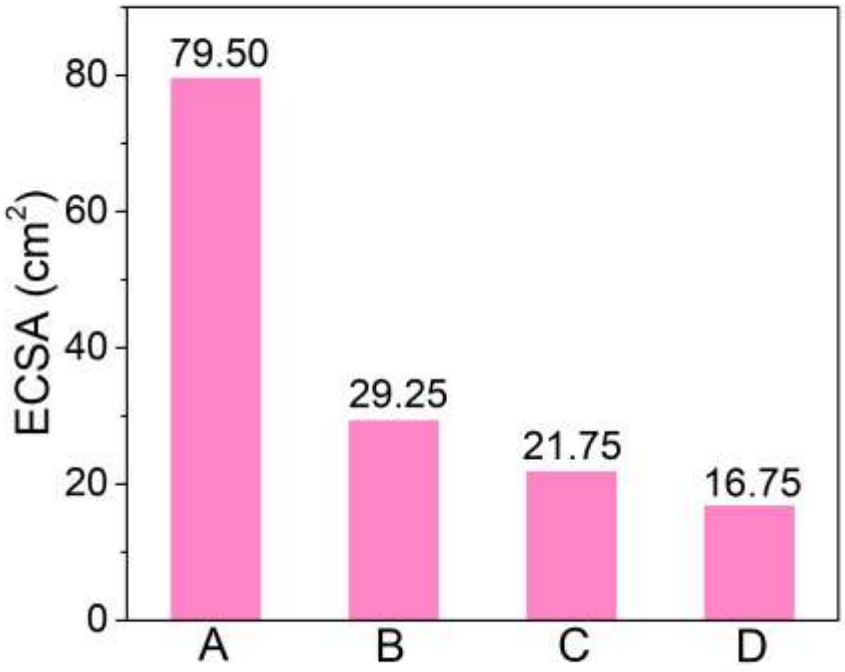

Fig. S23 The ECSA of each electrode is estimated by C_{dl}, where A is OH^-&Fe^{3+}-NMF, B is OH^-&Fe^{3+}-NF, C is NMF and D is NF.

According to the approximate value of double-layer capacitance, the ECSA of each electrode can be obtained by the following formula:

$$ECSA = \frac{C_{dl} \times A}{C_s}$$

Cs is a constant, Cs displays the electrolyte's certain capacitance that equals 0.04 mF cm^{-2} for the KOH solution.[1] From this, the ECSA values of OH^-&Fe^{3+}-NMF, OH^-&Fe^{3+}-NF, NMF and NF are 79.5 cm^2, 29.25 cm^2, 21.75 cm^2 and 16.75 cm^2, respectively. The ECSA value of OH^-&Fe^{3+}NMF is the highest, which can provide more active sites than other catalysts.

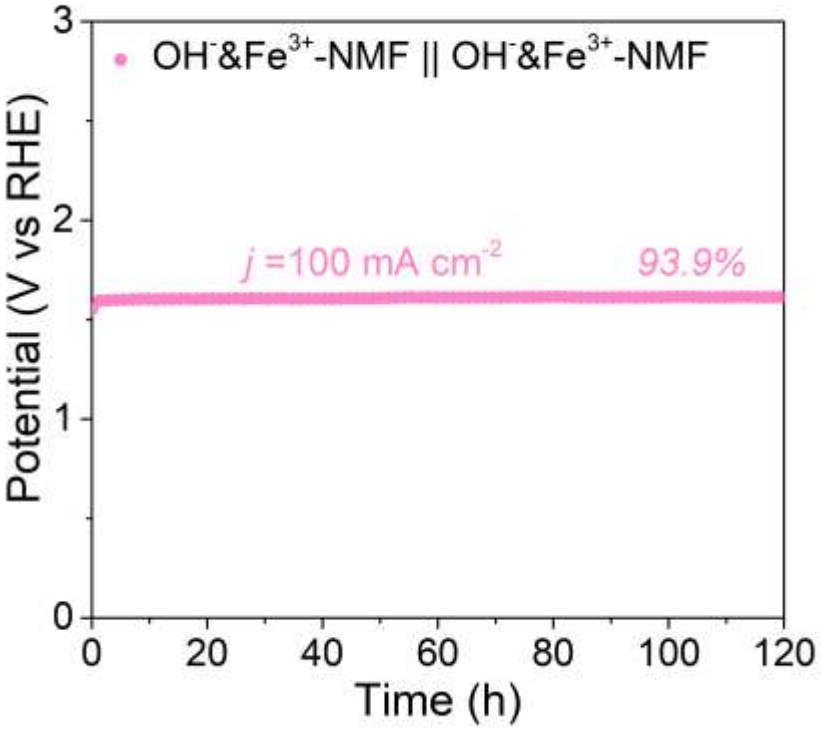

Fig. S24 CP stability test of OH^-&Fe^{3+}-NMF||OH^-&Fe^{3+}-NMF at the current density of 100 mA cm^{-2}.

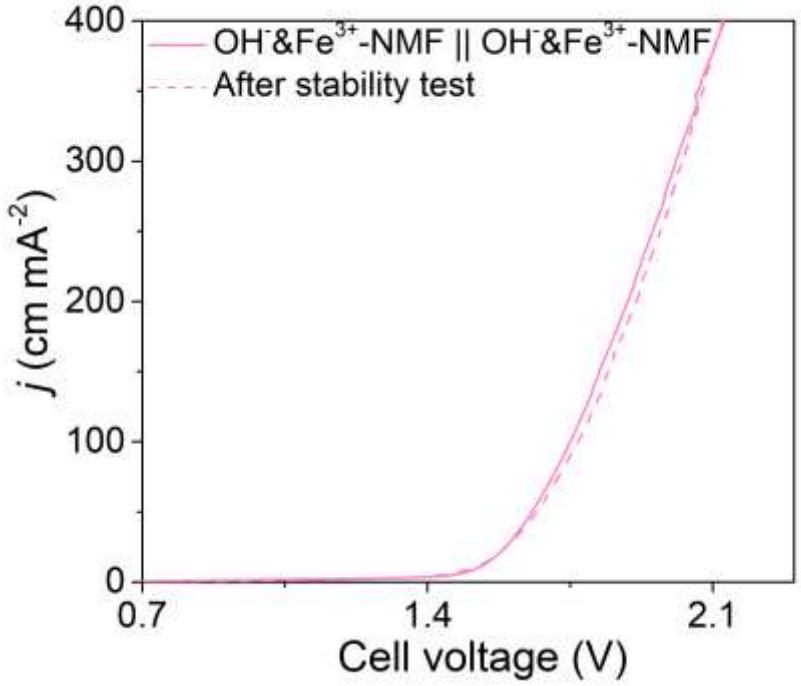

Fig. S25 Polarization curve of OH^-&Fe^{3+}-NMF || OH^-&Fe^{3+}-NMF after water splitting stability test for 120 h at current density of 100 mA cm^{-2}.

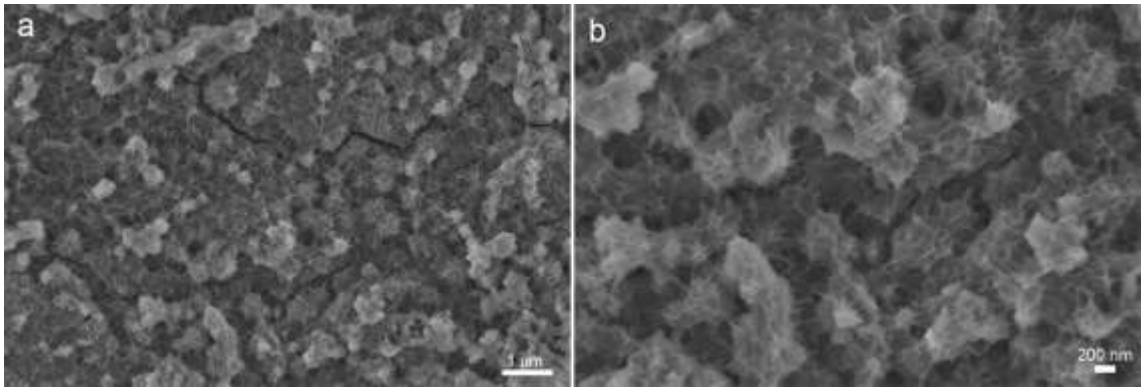

Fig. S26 SEM images of OH^-&Fe^{3+}-NMF after OWS stability test.

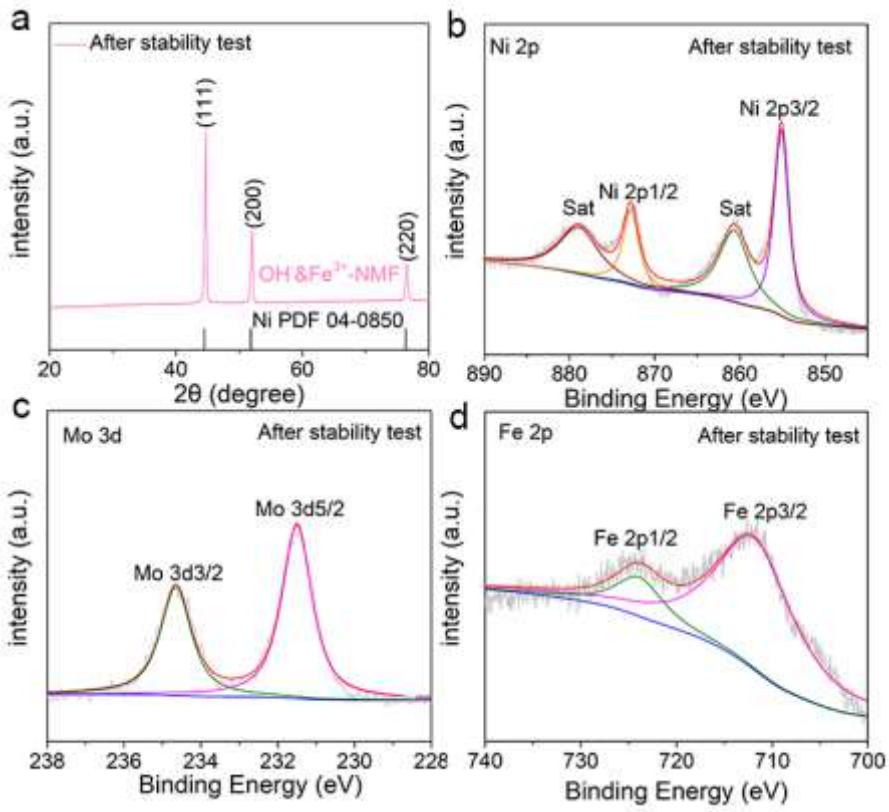

Fig. S27 (a) XRD characterization and XPS spectra of (b) Ni 2p, (c) Mo 3d and (d) Fe 2p for OH^-&Fe^{3+}-NMF electrode after OWS stability test.

Significantly, The SEM image of OH^-&Fe^{3+}-NMF after 120h long-term stability test reveals that its morphology remains intact and has almost no structure collapse (Fig. S26). This result illustrates that the coral-like nanosheet array structure is quite firm, and evidences the outstanding stability of OH^-&Fe^{3+}-NMF. Furthermore, the corresponding XRD characterization demonstrates that the integrity of the crystal

structure is well preserved (Fig. S27a). And not only that, there is also no obvious change in the chemical valence of the elements of OH^-&Fe^{3+}-NMF in the XPS spectrum. For Ni 2p spectrum of OH^-&Fe^{3+}-NMF (Fig. S27b), the peaks located at 855.4 eV and 873.1 eV can be attributed to Ni^{2+} $2P_{3/2}$ and Ni^{2+} $2P_{1/2}$, respectively, and the two peaks located at 861.1 and 878.6 eV are the satellite peaks of Ni 2p. In Fig. S27c, the spectra of Mo $3d_{5/2}$ (231.5 eV) and Mo $3d_{3/2}$ (234.7 eV) are attributed to Mo^{5+}. The Fe 2p peaks (Fig. S27d) at 711.9 eV and 724.6 eV correspond with Fe^{3+} $2p_{3/2}$ and Fe^{3+} $2p_{1/2}$. Consequently, we conclude that OH^-&Fe^{3+}-NMF has a stable structure. Thus, it shows satisfactory electrochemical stability of OWS after long periods stability test.

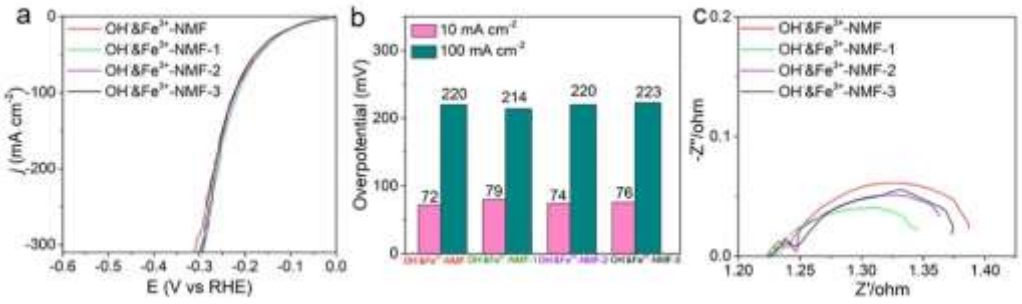

Fig. S28 (a) HER polarization curves of OH^-&Fe^{3+}-NMF, OH^-&Fe^{3+}-NMF-1, OH^-&Fe^{3+}-NMF-2, OH^-&Fe^{3+}-NMF-3. (b) Overpotentials obtained from polarization curves at the current density of 10 and 100 mA cm^{-2}. (C) EIS plots.

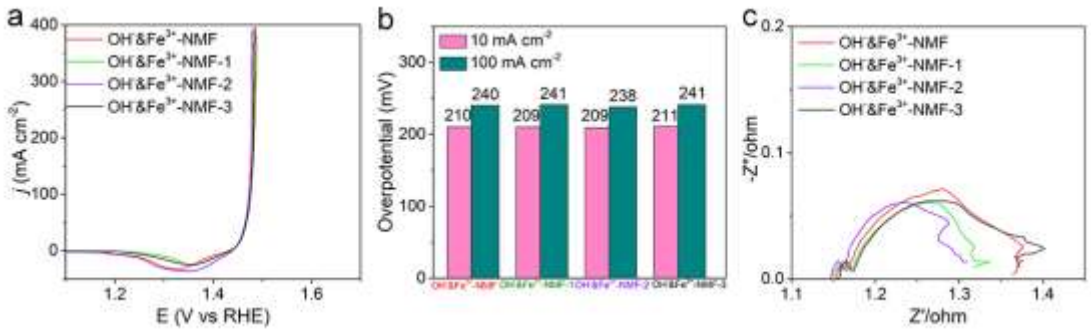

Fig. S29 (a) OER polarization curves of OH^-&Fe^{3+}-NMF, OH^-&Fe^{3+}-NMF-1, OH^-&Fe^{3+}-NMF-2, OH^-&Fe^{3+}-NMF-3. (b) Overpotentials obtained from polarization curves at the current density of 10 and 100 mA cm^{-2}. (C) EIS plots.

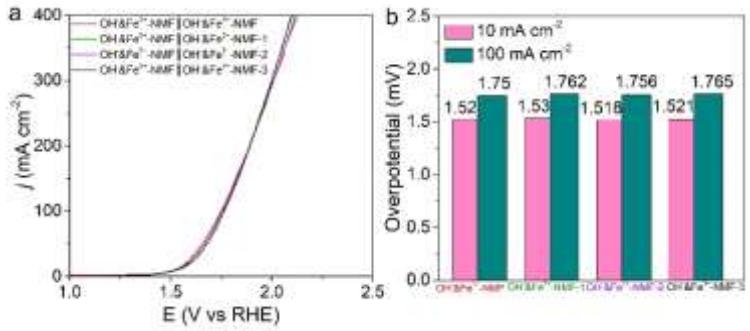

Fig. S30 (a) OWS polarization curves of OH^-&Fe^{3+}-NMF, OH^-&Fe^{3+}-NMF-1, OH^-&Fe^{3+}-NMF-2, OH^-&Fe^{3+}-NMF-3. (b) Overpotentials obtained from polarization curves at the current density of 10 and 100 mA cm^{-2}.

A series of repeatable electrochemical tests were performed on OH^-&Fe^{3+}-NMF. As depicted in Fig. S28a and S28b, the overpotential histograms of various electrodes at current densities of 10 and 100 mA cm^{-2} are listed according to LSV polarization curves. There is no obvious difference between the performance of new repeating groups (OH^-&Fe^{3+}-NMF-1, -2, and -3) and that of OH^-&Fe^{3+}-NMF (in main article text). In Fig. S28c, the corresponding EIS were in turn 0.0782 Ω for OH^-&Fe^{3+}-NMF-1, 0.0952 Ω for OH^-&Fe^{3+}-NMF-2, and 0.1069 Ω for OH^-&Fe^{3+}-NMF-3. These EIS values are comparable to that obtained for OH^-&Fe^{3+}-NMF (0.09 Ω). It was evident from Fig. S29a and S29b that the reproducibility was also excellent for OER performance test. The EIS values of various electrodes were in turn 0.114 Ω for OH^-&Fe^{3+}-NMF-1, 0.106 Ω for OH^-&Fe^{3+}-NMF-2, and 0.168 Ω for OH^-&Fe^{3+}-NMF-3 (Fig. S29c). It was observed that EIS values of the repetition groups were quite close to those of OH^-&Fe^{3+}-NMF (0.13 Ω). As shown in Fig. S30a and S30b, the OWS test was also repeated three times. The deviation range of performance values was small and reproducible.

Supplementary Tables

Tab. S1 Comparison of OER activity of OH^-&Fe^{3+}-NMF electrodes with reported OER catalysts.

Catalyst	Electrolyte	Overpotential at 10 mA cm^{-2} (mV vs RHE)	Tafel slope (mV dec^{-1})	Reference
OH^-&Fe^{3+}-NMF	1M KOH	210	34.1	This work
Ni/NiFeMoOx/NF	1M NaOH	255	35	2
NiFeMo/NF	1M KOH	230	59.9	3
Ni–Fe–Mo/NF	30wt.% KOH	306	77.1	4
NiMoN-450/NF	1M KOH	230	72	5
NF@NiMoCo	1M KOH	277	87	6
NiMo/NF	1M KOH	279	63	7
Mo-NiCoP/NF	1M KOH	262	49.4	8
FNMCO-6/NF	1M KOH	242	67.8	9
Ni/MoO_2@CN	1M KOH	250	48	10
$Mo_{0.6}$-$CoSe_2$ NS@NF	1M KOH	234	58	11

Tab. S2 Comparison of HER activity of OH^-&Fe^{3+}-NMF electrodes with reported HER catalysts.

Catalyst	Electrolyte	Overpotential at 10 mA cm^{-2} (mV vs RHE)	Tafel slope (mV dec^{-1})	Reference
OH^-&Fe^{3+}-NMF	1M KOH	72	49.7	This work
$NiMoO_4$-$Ni(OH)_2$/NF	1M KOH	93	97	12
NiMo/Cu-NS/NF-2	1M KOH	89	104	13
NiMo@ZnO/NF	1M KOH	110	131.2	14
NiMo MT/NF	1M KOH	119	119	15
NiMo/$NiMoO_4$@NC/NF	0.5 M H2SO4	80	98.9	16
NiFeMoS/NF-P	1M KOH	100	204	17
Ni-Fe-S-0.8/NF	1M KOH	142	133.3	18
Mo-doped Ni_3S_2	1M KOH	96	71	19
NF/$Co_{5.0}Mo_1P$/NiFe-LDH	1M KOH	98.9	93.3	20
Ni-Se-Mo/NF	1M KOH	101	98.9	21

Tab. S3 Comparison of Overall water splitting activity of OH^-&Fe^{3+}-NMF || OH^-&Fe^{3+}-NMF bifunctional electrodes with reported bifunctional catalysts.

Catalyst	Electrolyte	water splitting cell voltage (V) at 10 mA cm^{-2}	Substrate	Reference
OH^-&Fe^{3+}-NMF||OH^-&Fe^{3+}-NMF	1M KOH	1.52	NMF	This work
NiFeMo/NF||NiFeMo/NF	1M KOH	1.6	NF	3
NiMo@ZnO/NF||NiMo@ZnO/NF	1M KOH	1.718	NF	14
$Ni_5Mo/NiCo_2O_4$/NF||$Ni_5Mo/NiCo_2O_4$/NF	1M KOH	1.54	NF	22
NiMo-NWs/Ni-foam||NiFe-LDH/Ni-foam	1M KOH	1.53	NF	23
NF@NiMoCo||NF@NiMoCo	1M KOH	1.56	NF	6
Ni-Fe/$NiMoN_x$/NF||Ni-Fe/$NiMoN_x$/NF	1M KOH	1.54	NF	24
Ni-Fe-Sn/NF||Ni-Fe-Sn/NF	1M KOH	1.55	NF	25
Ni-Fe-S/NF||Ni-Fe-S/NF	1M KOH	1.59	NF	26
Mo-NiCoP/NF||Mo-NiCoP/NF	1M KOH	1.56	NF	8
FNMCO-6/NF||FNMCO-6/NF	0.1M PBS	1.679	NF	9

References

1. A. A. Shah, M. Kumar, U. Aftab and M. I. Abro, *Chemical Engineering & Technology*, 2022, **45**, 1-8.
2. Y. K. Li, G. Zhang, W. T. Lu and F. F. Cao, *Adv Sci (Weinh)*, 2020, **7**, 1902034-1902143.
3. Z. Lv, Z. Li, X. Tan, Z. Li, R. Wang, M. Wen, X. Liu, G. Wang, G. Xie and L. Jiang, *Applied Surface Science*, 2021, **552**, 149514-149520.
4. Y. Huang, Y. Wu, Z. Zhang, L. Yang and Q. Zang, *Electrochimica Acta*, 2021, **390**, 138754-138761.
5. Y. Wang, Y. Sun, F. Yan, C. Zhu, P. Gao, X. Zhang and Y. Chen, *Journal of Materials Chemistry A*, 2018, **6**, 8479-8487.
6. K. Hu, M. Wu, S. Hinokuma, T. Ohto, M. Wakisaka, J.-i. Fujita and Y. Ito, *Journal of Materials Chemistry A*, 2019, **7**, 2156-2164.
7. Y. Wang, Y. Wang, J. Bai and W. M. Lau, *ChemistrySelect*, 2022, **7**, e20220468-e20220474.
8. Y. Zhao, J. Chen, S. Zhao, W. Zhou, R. Dai, X. Zhao, Z. Chen, T. Sun, H. Zhang and A. Chen, *Journal of Alloys and Compounds*, 2022, **918**, 165802-165809.
9. H. Shi, Q. Zha and Y. Ni, *Journal of Alloys and Compounds*, 2022, **904**, 164052-164060.
10. G. Qian, J. Chen, T. Yu, J. Liu, L. Luo and S. Yin, *Nanomicro Lett*, 2021, **14**, 20-34.
11. J. Huang, S. Wang, J. Nie, C. Huang, X. Zhang, B. Wang, J. Tang, C. Du, Z. Liu and J. Chen, *Chemical Engineering Journal*, 2021, **417**, 128055-128064.
12. S. Hu, H. Wu, C. Feng and Y. Ding, *International Journal of Hydrogen Energy*, 2020, **45**, 21040-21050.
13. Z. Chang, L. Zhu, J. Zhao, P. Chen, D. Chen and H. Gao, *International Journal of Hydrogen Energy*, 2021, **46**, 3493-3503.
14. J. Cao, H. Li, R. Zhu, L. Ma, K. Zhou, Q. Wei and F. Luo, *Journal of Alloys and Compounds*, 2020, **844**, 155382-155388.
15. J. Cao, H. Li, J. Pu, S. Zeng, L. Liu, L. Zhang, F. Luo, L. Ma, K. Zhou and Q. Wei, *International Journal of Hydrogen Energy*, 2019, **44**, 24712-24718.
16. K. Karuppasamy, V. R. Jothi, D. Vikraman, K. Prasanna, T. Maiyalagan, B.-I. Sang, S.-C. Yi and H.-S. Kim, *Applied Surface Science*, 2019, **478**, 916-923.
17. K.-L. Yan, J.-F. Qin, Z.-Z. Liu, B. Dong, J.-Q. Chi, W.-K. Gao, J.-H. Lin, Y.-M. Chai and C.-G. Liu, *Chemical Engineering Journal*, 2018, **334**, 922-931.
18. Z. Zhang, Y. Wu and D. Zhang, *International Journal of Hydrogen Energy*, 2022, **47**, 1425-1434.
19. S. Li, J. Fan, S. Li, H. Jin, W. Luo, Y. Ma, J. Wu, Z. Chao, N. Naik, D. Pan and Z. Guo, *ES Energy & Environment*, 2022, **16**, 15-25.
20. W. Mai, Q. Cui, Z. Zhang, K. Zhang, G. Li, L. Tian and W. Hu, *ACS Applied Energy Materials*, 2020, **3**, 8075-8085.
21. Y. Gao, H. He, W. Tan, Y. Peng, X. Dai and Y. Wu, *International Journal of Hydrogen Energy*, 2020, **45**, 6015-6023.
22. H. Chen, S. Qiao, J. Yang and X. Du, *Molecular Catalysis*, 2022, **518**, 112086-112093.
23. M. Fang, W. Gao, G. Dong, Z. Xia, S. Yip, Y. Qin, Y. Qu and J. C. Ho, *Nano Energy*, 2016, **27**, 247-254.
24. Y. Qiu, M. Sun, J. Cheng, J. Sun, D. Sun and L. Zhang, *Catalysis Communications*, 2022, **164**, 106426-106433.
25. S. You, Y. Wu, Y. Wang, Z. He, L. Yin, Y. Zhang, Z. Sun and Z. Zhang, *International Journal of*

Hydrogen Energy, 2022, **47**, 29315-29326.

26. X. Yang, R. Qiu, M.-J. Lan, G. Chen, W. Xu and Y. Shen, *International Journal of Hydrogen Energy*, 2022, **47**, 36556-36565.